Chinese Journal of Polymer Science Vol. 32, No. 9, (2014), 1188–1198

Chinese Journal of Polymer Science
© Chinese Chemical Society
Institute of Chemistry, CAS
Springer-Verlag Berlin Heidelberg 2014

Preparation of Long-range Ordered Nanostructures in Semicrystalline Diblock Copolymer Thin Films Using Micromolding*

Peng Zhang[a, b], Hai-ying Huang[a], Yu Chen[c], Shun Yu[b], Christina Krywka[d, e], Sarathlal K. Vayalil[b], Stephan V. Roth[b**] and Tian-bai He[a**]

[a] *State Key Laboratory of Polymer Physics and Chemistry, Changchun Institute of Applied Chemistry, Chinese Academy of Sciences, Changchun 130022, China*

[b] *Deutsches Elektronen-Synchrotron, Hamburg D-22607, Germany*

[c] *Institute of High Energy Physics, Chinese Academy of Sciences, Beijing 100049, China*

[d] *Institute for Applied and Experimental Physics, University of Kiel, Kiel D-24118, Germany*

[e] *Institute of Materials Research, Helmholtz Zentrum Geesthacht, D-21502 Geesthacht, Germany*

Abstract Long-range ordered nanostructures are prepared in the poly(styrene)-block-poly(ε-caprolactone) diblock copolymer thin films using micromolding. We evaluated the change in crystallinity based on grazing-incidence X-ray diffraction and proved that the crystallinity increased with the decrease of the mold size. This means that ordered nanostructures with atomic length scale order can be adjusted by tuning the mesoscale confinement. The inherent mechanism was the cooperation of geometric confinement, microphase structure and surface-induced ordering of PS-*b*-PCL in the melt, which paved the way for the subsequent crystal growth. These findings establish a route to promote the cost-effective nanofabrication by combining the mature microfabrication technique with the emerging directed self-assembly of block copolymers.

Keywords: Long-range ordered nanostructure; Directed self-assembly; Surface-induced ordering; X-ray.

Electronic Supplementary Material Supplementary material is available in the online version of this article at http://dx.doi.org/10.1007/s10118-014-1506-x.

INTRODUCTION

Exploring polymer crystallization is fundamental as many commercially important polymers such as polyethylene, polypropylene, and poly(ε-caprolactone) are crystalline. The crystalline order reflects the periodic order on the atomic length scale, and this makes it very attractive for the fabrication of ultra-high density media, electric and photovoltaic devices[1–5]. However, the crystallization of polymers is notoriously hard to control. This is due to its sensitivity to external field and the inherent hierarchically assembled structures, which range from the atomic length scale *via* the molecular chain to the micrometer-scale spherulites.

* This work was financially supported by the National Natural Science Foundation of China (Nos. 21274148 and 21074135). The experimental setup at the Nanofocus Endstation of MiNaXS was funded by the German Federal Ministry of Education and Research (projects BMBF 05KS7FK1 and 05K10FK3).

** Corresponding authors: Stephan V. Roth, E-mail: stephan.roth@desy.de
Tian-bai He (何天白), E-mail: tbhe@ciac.ac.cn

Invited paper for the special issue of "Polymer Crystallization"
Received March 18, 2014; Revised April 28, 2014; Accepted May 9, 2014
doi: 10.1007/s10118-014-1506-x

To regulate the polymer crystallization, several strategies such as microphase separation in block copolymers, filling of inorganic nanopores and nanoimprinting were applied[6–10]. All of the above mentioned strategies have to tackle the influences of the interface. In some cases, the interface interaction will weaken the space control ability of the mold. For example, in nanoimprinted polymer thin films, partially confined crystallization occurred, because the affinity of polymers and substrates causes the formation of a residual layer near the substrate during imprinting[10, 11]. To overcome this obstacle, one can make use of the interface-induced ordering and let it serve for spatially controlled crystallization.

Recently, the combination of the traditional optical lithography with block copolymer self-assembly has been applied to achieve directed self-assembly and cost-effective nanofabrication[12–17]. The interface-induced ordering of block copolymers is a key factor for the success of directed self-assembly[6, 15, 16, 18]. Accordingly, using the inexpensive mesoscale mold fabricated by optical lithography for directing the organization of semicrystalline diblock copolymer would be a cost-effective way to control the polymer crystallization[6]. In our previous work, we successfully prepared the long-range ordered crystalline structure in the micromolded poly(butadiene)-block-poly(ε-caprolactone) (PB-*b*-PCL) thin film, where we inferred that the geometric effect of mold influenced the ordering of microphase structure and the following growth of the crystal[19].

In this study, we focus on exploring the long-range ordered nanostructures in a micromolded semicrystalline diblock copolymer thin film. Poly(styrene)-block-poly(ε-caprolactone) (PS-*b*-PCL) was selected because it established the following several advantages: Firstly, the surface structure evolution of the PS-*b*-PCL diblock copolymer thin film at high temperatures was well explored based on *in situ* observation[20]. Secondly, PS-*b*-PCL exhibits hard-confined crystallization, *i.e.*, glass transition temperature of the amorphous block is higher than the melting point of the crystalline block. Hence it offers the possibility to investigate the influence of imprinting on the microphase structure, because the crystal is confined in the vitreous PS block[9, 20, 21]. Finally, the dominant electron density difference is observed in PS and the crystalline PCL rather than the PS and the amorphous PCL. Therefore the change in crystallinity in PS-*b*-PCL can easily be detected by X-rays[21–24]. Moreover, X-ray nanobeams enable detecting the ordering of nanostructures in a single grating line.

EXPERIMENTAL SECTION

Materials

The PS-*b*-PCL (number average molecular weight, M_n = 18500 g/mol, polydispersity index, PDI = 1.13, and volume fraction of PCL is 46%) and PCL (M_n = 10000 g/mol and PDI = 1.4) thin films were spun-cast from toluene solution (10 mg/mL) onto clean silicon wafers and then removed the solvent by high vacuum treatment for 24 h. The thickness of the as-prepared PS-*b*-PCL thin film was evaluated by scratching method with AFM and the value is ~42 nm.

Micromolding

The imprinting mold used in this study was PDMS (Sylgard 184, Dow Corning Co.) replicated from the aluminum-based master mold. The PDMS stamp consists of parallel line-grating patterns with varied periodicities, namely, 833, 566 and 420 nm. The crest height is 120 nm. The imprinting was performed in a homemade imprinter. The sample was heated to 150 °C and annealed for 20 min, then imprinted at 150 °C and kept for 10 min before cooled to 40 °C at ~5 K/min. It was kept at 40 °C for 24 h to crystallize, after which the pressure (0.3 MPa) was released and the mold was removed. To give a clear illustration and distinctiveness, the sample was named after the periodicity value of the mold, *e.g.*, the sample imprinted with 833 nm mold was named S-833. As a comparison, the thermal-annealed sample was treated under the same heat treatment protocol without imprinting.

Atomic Force Microscopy

The atomic force microscopy (AFM) data were acquired in air with an Agilent 5500 AFM (Agilent Technologies Inc., Santa Clara, CA) operated in taping mode. The silicon cantilevers (OMCL-AC160TS, Olympus Co.) with a resonance frequency of ~300 Hz and a spring constant of about 42 N/m were used.

X-ray Diffraction and Scattering

The grazing-incidence X-ray diffraction (GIXRD) data were obtained at 1W1A beamline of Beijing Synchrotron Radiation Facility (BSRF), using a Huber 5-circle diffractometer and a point detector. The X-ray wavelength and the beam size were 0.154 nm and 0.7 mm × 0.4 mm (horizontal × vertical), respectively. The geometry of GIXRD experiments is schematically presented in Fig. 1(a). The α_i, and α_d represent the incident and diffraction angles, respectively and Φ is the azimuthal angle. The angle α_i was fixed at 0.16°. The PS-*b*-PCL thin film was first aligned with the long-axis of the trenches parallel to the incident X-ray, and then GIXRD was measured at a step-scan rate of 1 s at each 0.05° step. The scattering angle 2θ was ranging from 5° to 30°. The Φ scanning was performed after the 2θ scanning with the 2θ positions locked to 21.3° ((110) plane) and 23.6° ((200) plane). The step-scan rate was 1 s at each 1° step. The plane spacing was calculated using the Bragg equation, $n\lambda = 2d\sin\theta$, where n is the diffraction order, λ is the wavelength, d is the plane spacing and θ is the diffraction angle. The diffracted angle was calibrated by powder diffraction of monocrystalline silicon which has an intense (400) reflection at $2\theta = 69.13°$.

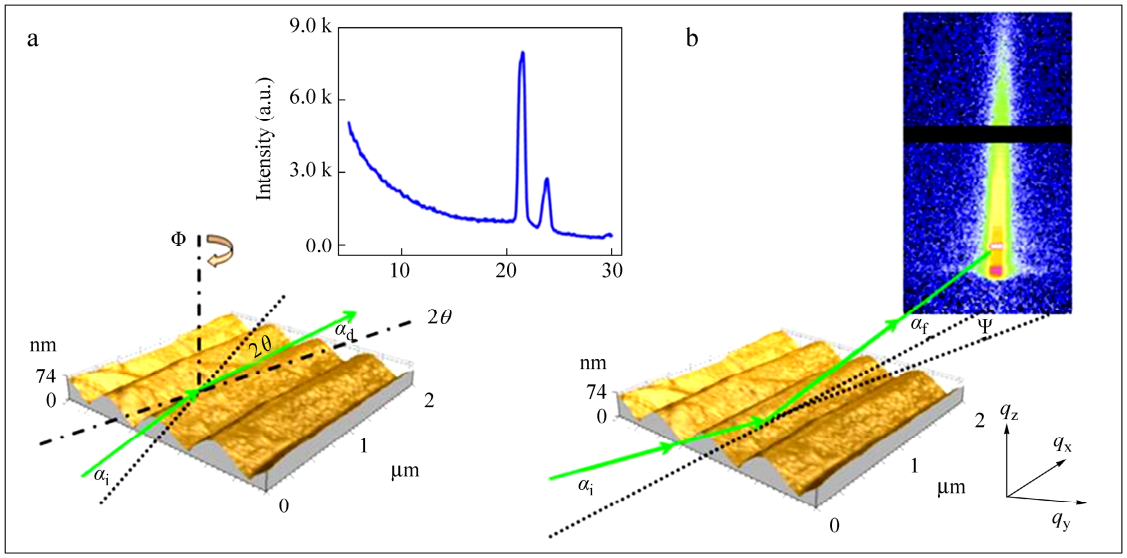


Fig. 1 (a) Schematic drawings of the in-plane grazing incidence X-ray diffraction (GIXRD) measurement and the corresponding 1D line curve; (b) Schematic drawing of the nanobeam grazing incidence small-angle X-ray scattering (nGISAXS) measurement and the corresponding 2D patterns

The grazing incidence small-angle X-ray scattering experiments (GISAXS) were performed at the nanofocus endstation of P03 beamline at PETRA III of the Deutsches Elektronen Synchrotron (DESY) in Hamburg, Germany[25]. The X-ray wavelength and the beam size were 0.0957 nm and 500 nm × 250 nm (horizontal × vertical), respectively. A PILATUS 1M (Dectris Ltd., Switzerland) detector was employed to collect 2D GISAXS patterns. The sample-to-detector distance calibrated using silver behenate to 957 ± 1 mm. As shown in Fig. 1(b), the Ψ, α_i and α_f represent out-of-plane angle, incident angle and exit angle, respectively. α_i was set to 0.3°. The analysis of the 2D GISAXS images was performed in terms of the horizontal scattering vector $q_y = 2\pi\,(\sin\Psi\cos\alpha_f)/\lambda$ and the vertical scattering vector $q_z = 2\pi(\sin\alpha_i + \sin\alpha_f)/\lambda$[26].

RESULTS AND DISCUSSION

The morphological change of PS-*b*-PCL thin films before and after micromolding is shown in Fig. 2. In the as spun sample (Fig. 2a) randomly oriented crystals are found. In the imprinted samples the material graphoepitaxially aligns along the trenches, and lamellae cover the crests (Figs. 2c and 2d). These are quite different from the thermally annealed samples where, under the function of dewetting and microphase

separation, droplets and superimposed lamellae are observed[20]. In addition, by observing the height images of the imprinted samples in Fig. 1 and Figs. 2b–2d, it seems that the surface crystallization occurred leading to a roughened crest. This is in line with the surface crystallization behavior in thermally annealed PS-*b*-PCL thin films, visualized by the AFM measurements of the crystal growth at T = 40 °C (see S1 of Supporting Information).

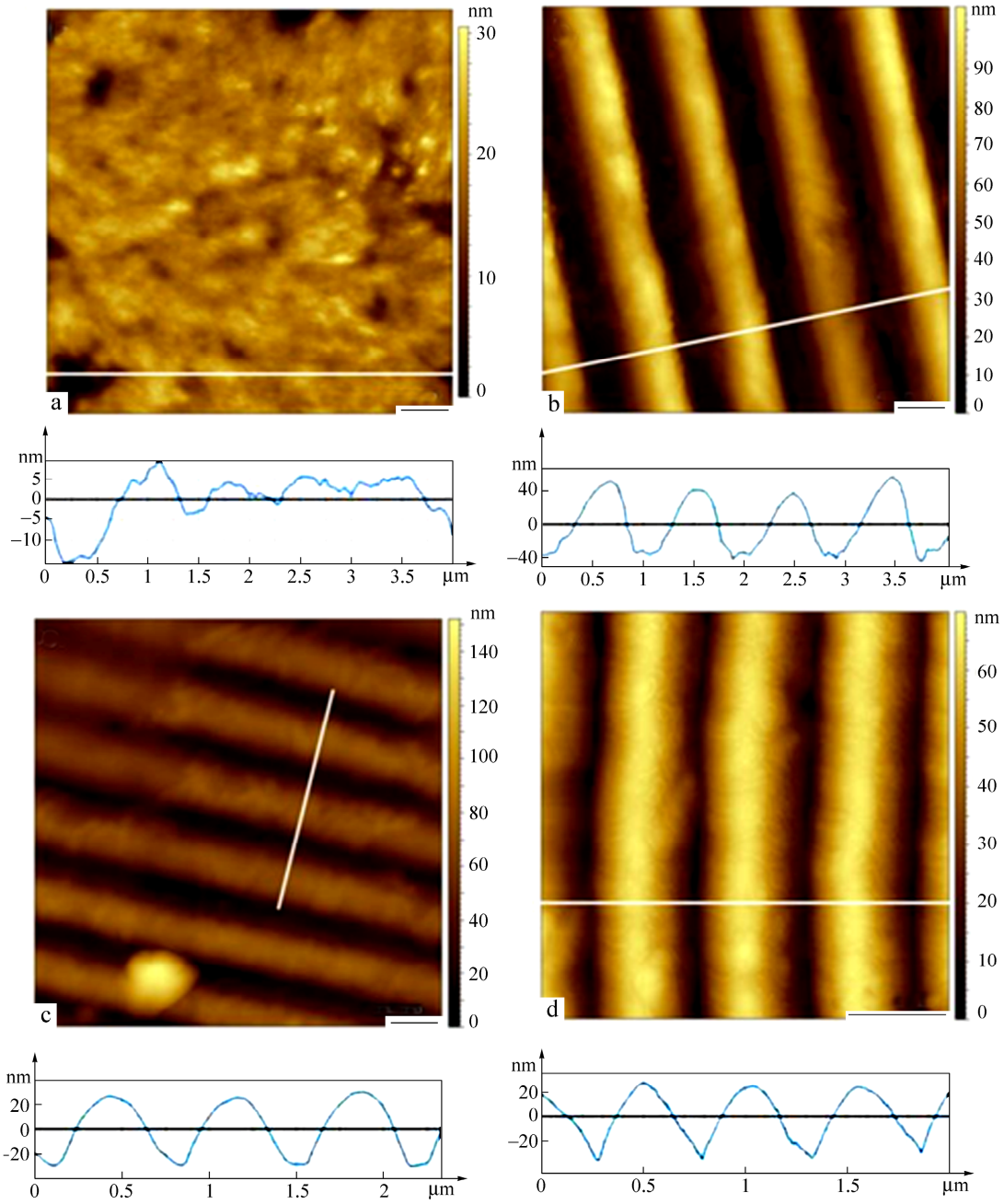


Fig. 2 AFM height images of PS-*b*-PCL thin films: (a) As spun, (b) S-833, (c) S-566 and (d) S-420 The line profiles relate to the height fluctuations at the corresponding cross sections. The inserted scale bars in the lower right corner indicate 500 nm.

As the incident angle α_i = 0.16° is slightly larger than the critical angle for total reflection $\alpha_{c,\ PS\text{-}b\text{-}PCL} \approx$ 0.157°, the penetration depth is larger than the film thickness (see S2 of Supporting Information). Hence the GIXRD results clearly show the crystallization information not restricted to the surface. Besides, α_i is below the critical angle of the substrate $\alpha_{c,\ (SiOx/Si)}$ = 0.23°; therefore, the scattering from the substrate was reduced compared to that from the thin film. Figure 3 shows in-plane GIXRD patterns measured at α_i = 0.16° for the PS-*b*-PCL thin film before (Fig. 3a) and after micromolding (Fig. 3b–3d). It should be noted that the crystalline lamellae feature is too weak to be distinguished from the background under out-of-plane mode. This implies that there are negligible edge-on (chain stems parallel to the substrate) crystalline lamella found in the sample. Therefore, the GIXRD experiments were performed in in-plane mode as shown in Fig. 1(a). Furthermore, we can infer that crystallographic *c*-axis (chain stems) of PCL is perpendicular to the substrate. Considering the anisotropy of imprinting-induced material flow, the detection was performed in both parallel (P) and normal (N) to the long axis of the trenches (LA). As shown in Figs. 3(b)–3(d), the intensity of crystalline peaks increases with the decrease of the trench size. Moreover, in the N direction, only one peak is observed which is centered at 21.3°. In contrast, there are two obvious peaks centered at 21.3° and 23.6°, respectively found in P direction. This means that the PCL crystals have anisotropic arrangement. Using Bragg's equation and the lattice constants of the orthorhombic PCL unit cell *a* = 0.745 nm, *b* = 0.498 nm and *c* = 1.705 nm[22], we can attribute the diffraction peaks at 21.3° and 23.6° to the reflections of (110) and (200) planes, respectively. Moreover, we can ascertain that the crystallographic *a*- and *b*-axes are normal and parallel to LA, respectively. This is consistent with the GIXRD out-of-plane results.

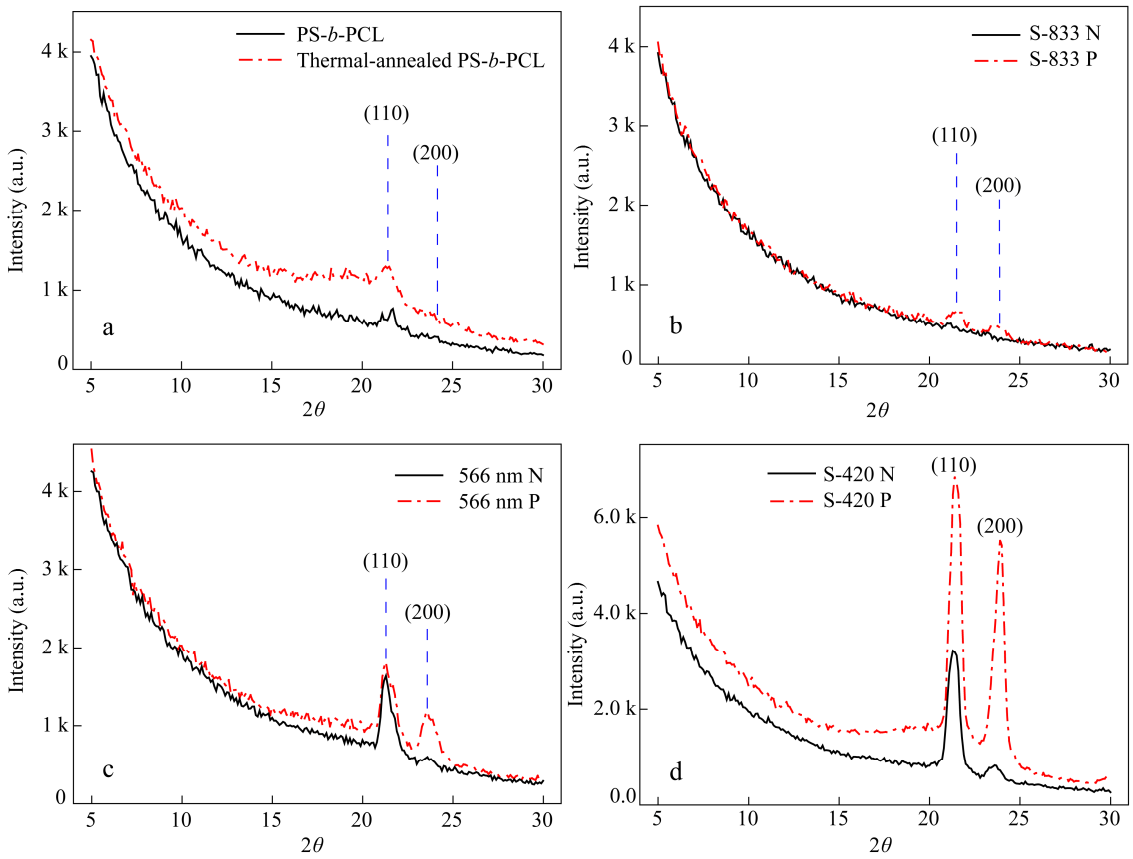


Fig. 3 Intensity profiles of the in-plane GIXRD patterns measured at α_i = 0.16° for the (a) as spun and thermal-annealed PS-*b*-PCL thin films, (b) S-833, (c) S-566 and (d) S-420
N and P indicate the incident X-ray beam being normal or parallel to the long axis of trenches, respectively.

In order to characterize the anisotropic orientation of the PCL crystals, the imprinted samples were scanned azimuthally. The azimuthal dependent intensity profiles of the S-566 and S-420 are shown in Fig. 4. In the azimuthal intensity profiles in Figs. 4(a)–4(d), we find that the (110) reflection displays four separated arcs and the (200) reflection two separated arcs. Quriam *et al*. predicted that, in the ideal case, the (110) maxima should be separated by an azimuthal angle of 116° across the equator[27]. The measured azimuthal separation angles (δ, as shown in Fig. 5) for the S-566 and S-420 are 110° and 122°, respectively. The values were obtained by fitting a Gaussian function to each diffraction peak. The experimental δ values agree well with the ideal values[27, 28] and are comparable to the experimental results in the nanoscale cylinders such as PB-*b*-PCL[19], PS-*b*-PCL[21] and PE-block-poly(3-methyl-1-butene)[27]. This indicates that the hierarchical confinement in imprinted PS-*b*-PCL thin films can take similar role as the nanoscale cylinders in directing the crystal growth. According to the azimuthal results, we can retract the arrangement of the crystal and the confinement from the mold. As shown in Fig. 5, well-ordered PCL crystals are prepared in the imprinted PS-*b*-PCL thin film.

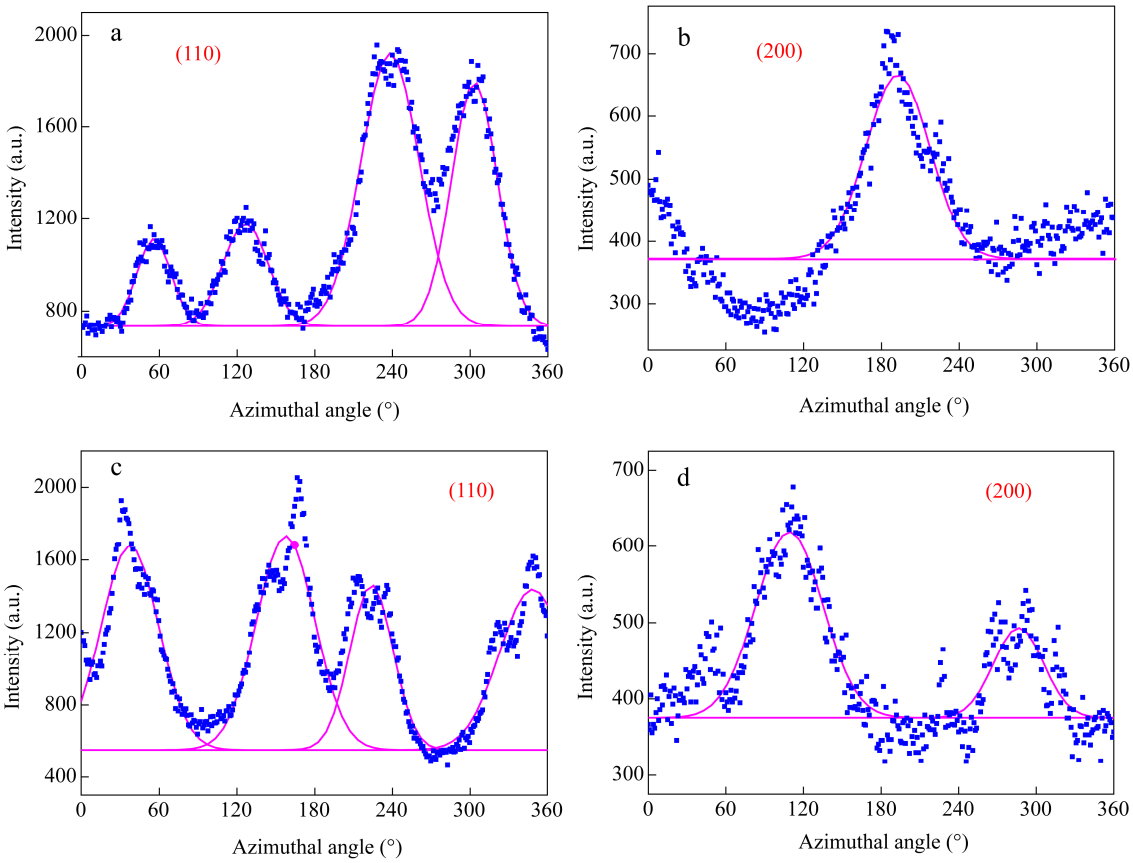


Fig. 4 Azimuthal dependent intensity profiles of the (110) and (200) reflections for (a and b) S-566 and (c and d) S-420
It should be noted that the initial scanning positions in panels (a) and (b) are orthogonal to the long axis of the trench (LA) while those in panels (c) and (d) are parallel to LA. The peaks were fitted each with a Gaussian function as indicated with the solid lines.

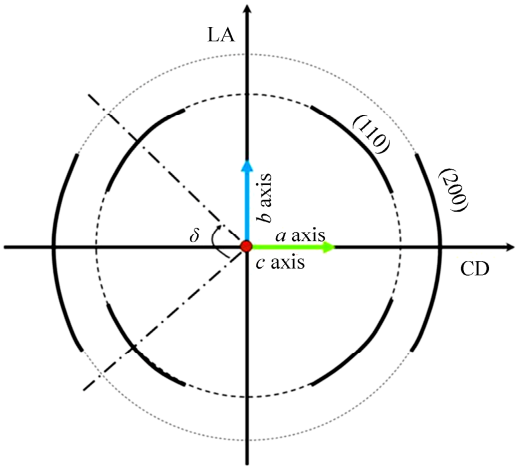


Fig. 5 Schematic diagram of the crystallographic pattern with indexed reflections and the confinement resulting from the mold
The crystallographic *c*-axis is vertical to this image, CD and LA represents the confined direction and the long axis of the trenches, respectively. The adjacent peak centers of (110) plane make an azimuthal angle δ about the equator.

To further explore the influence of the trench size on the crystallization of PS-*b*-PCL, the normalized maximum peak intensities from the intensity profiles in Fig. 3 are presented in Table 1. Compared to the as spun sample, enhanced crystallinity is observed in the thermal-annealed one. This could be reconciled by the fact that the reorganization of the microphase structure during annealing released the frozen PCL[28]. In the thermal-annealed PS-*b*-PCL, the PCL crystal tends to extend parallel with the substrate because it is confined by the microphase structure in the orthogonal direction[20]. This explains why only flat-on lamellae were detected with the GIXRD. Moreover, in the imprinted PS-*b*-PCL, the I_{110} in both N and P directions and I_{200} in P direction increase with the decrease of the mold periodicity while there is no regular change for I_{200} in N direction. Taking into consideration that the crystallographic *b*-axis is the fast growth direction of PCL, we can understand its extension along LA due to unimpeded growth and more available crystallizable material in that direction[29]. However, this finding is quite different from the generally accepted model, namely, the polymer crystallinity will decrease due to the space confinement[7, 8, 21]. The decrease of crystallinity due to spatial confinement is also reflected in the S-833 and micromolded PCL samples as shown in Table 1. Compared to the thermal-annealed PS-*b*-PCL, S-833 shows a lower crystallinity. Furthermore, the crystallinity of micromolded PCL samples decreases in both N and P directions decreasing mold periodicity. Thus, we can infer that the enhanced crystallinity of micromolded PS-*b*-PCL samples can be related to the ordered microphase structure. This ordered microphase structure counterbalances the decrease of crystallinity resulting from spatial confinement.

Table 1. Normalized peak intensities (I^a) of (110) and (200) with respect to the change of trench size for the incident X-ray normal (N) and parallel (P) to the LA

	PS-*b*-PCL		PCL	
	I_{110}	I_{200}	I_{110}	I_{200}
as spun	0.024	0.016	0.663	0.223
thermal-annealed	0.058	0.039		
S-833 P	0.055	0.035	0.208	0.11
S-566 P	0.095	0.062	0.181	0.05
S-420 P	0.233	0.189		
S-833 N	0.026	0.021	0.543	0.112
S-566 N	0.086	0.032	0.232	0.09
S-420 N	0.109	0.028		

[a] The normalized intensity was calculated by dividing the detector value with the incident photon flux value

In order to prove our assumption and address the function of the microphase structure, we used nanobeam GISAXS (nGISAXS) which already was successfully applied to study the structures of polymer thin films[30–33]. In our case the electron densities for the PCL crystals and amorphous PS blocks are 393 and 340 e/nm^3, respectively[23, 34]. This makes nGISAXS a suitable method for the analysis of PS-*b*-PCL thin films. To detect the microphase structure of the PS-*b*-PCL thin films, the α_i was set at 0.3° which is bigger that the α_c of PS-*b*-PCL (0.098°, see S3 of supporting information). By choosing the S-833, for which the periodicity value is larger than the beam size, we can focus on the microphase structure orientation in a single grating line.

Figure 6 shows the nGISAXS patterns of the imprinted and thermal-annealed PS-*b*-PCL thin films. The thermal-annealed sample without imprinting is presented as a comparison. The prominent feature in the nGISAXS pattern consists of a vertical intensity streak showing that the regular structure exists only in the direction normal to the substrate[35]. This is in line with our GIXRD experimental results where only flat-on crystals were detected in PS-*b*-PCL thin films. We attributed these findings to the fact that PCL wets the substrate and amorphous lamellae in the PS-*b*-PCL thin film are formed parallel to the substrate[20]. Moreover, as shown in Figs. 6(a) and 6(b), the nGISAXS patterns show several ordered intensity stripes in the vertical direction in the imprinted sample. In contrast, as shown in Fig. 6(c), such features are absent in the thermal-annealed PS-*b*-PCL thin film.

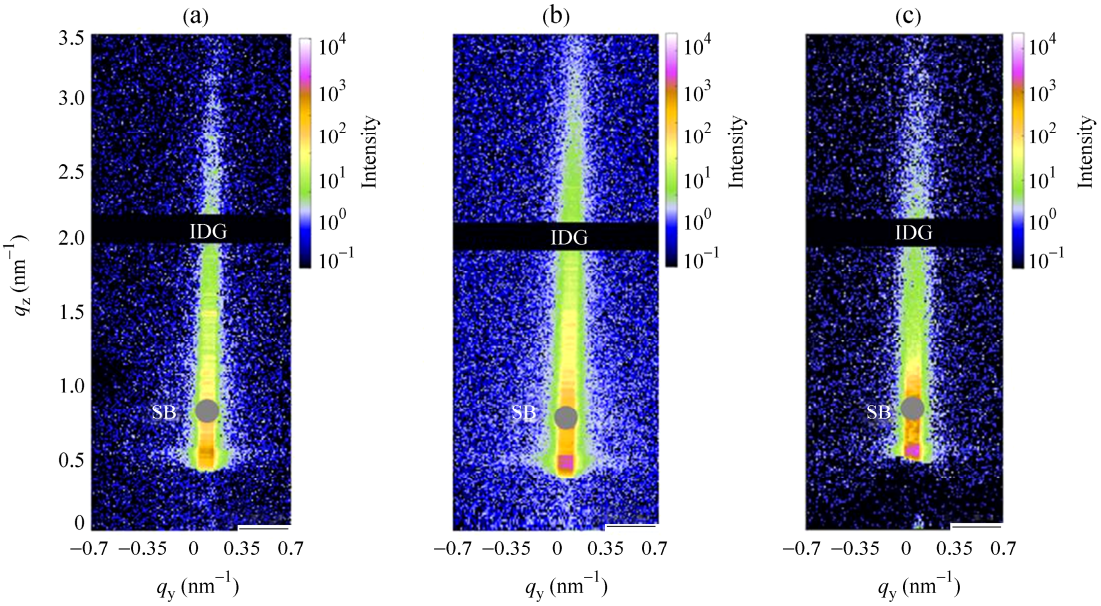


Fig. 6 Representative nGISAXS patterns of the PS-*b*-PCL thin films: (a) S-833 with the incident X-ray parallel to the LA, (b) S-833 with the incident X-ray normal to the LA and (c) thermal-annealed sample The scale bars indicate 0.35 nm^{-1}. The specular beam position (SB) is blocked to show better contrast. The black stripe is caused by the gap between the modules of the detector (IDG).

To characterize these stripes, Fig. 7 presents the intensity as a function of q_z around $q_y = 0$. For the analysis of the imprinted samples as shown in Figs. 7(a) and 7(b), we marked the periodic features with dotted lines. We confirm that the ordered lamellae structure exists in the imprinted PS-*b*-PCL thin films because one finds nearly equally spaced adjacent peaks. We find a lamellar periodicity of d_{lam} = 25.4 ± 1.3 nm. As the electron density difference in PS-*b*-PCL is mainly resulting from PS and crystallized PCL[20, 21], we can attribute this value to the periodicity of crystallized PS-*b*-PCL[36].

As shown in Fig. 7(c), no regular sharp peak is observed in the thermal-annealed PS-*b*-PCL thin film. This means it has a much less regular structure than the S-833. As shown in Table 1, thermally annealed PS-*b*-PCL has similar crystallinity with the S-833. The absence of the regular stripes (Fig. 6c) and a lamellar signal

(Fig. 7c) in the thermal-annealed PS-*b*-PCL thin film could then be attributed to the irregular arrangement of the PS and crystalline PCL layers. This could be rationalized by the dewetting induced rupture of the film. The material aggregates into droplets (see S3 of Supporting Information). Concerning the S-833, the dewetting of PS-*b*-PCL is inhibited by the mold and the material flow is influenced by the geometric confinement, thus well aligned grating structure is observed in Fig. 2(b). The structure difference between thermal-annealed PS-*b*-PCL and S-833 is also corroborated with the change of Yoneda peaks (q_z = 0.55). As shown in Fig. 7(c), a slim Yoneda peak resulting from the substrate is observed while, as shown in Figs. 7(a) and 7(b), several shoulder peaks around the Yoneda peak resulting from the polymer and silicon substrate are observed. The shoulder peaks in Figs. 7(a) and 7(b) are resulting from the Yoneda peak of PS-*b*-PCL and it is the reflection of the enhanced electron density difference between PS and crystallized PCL.

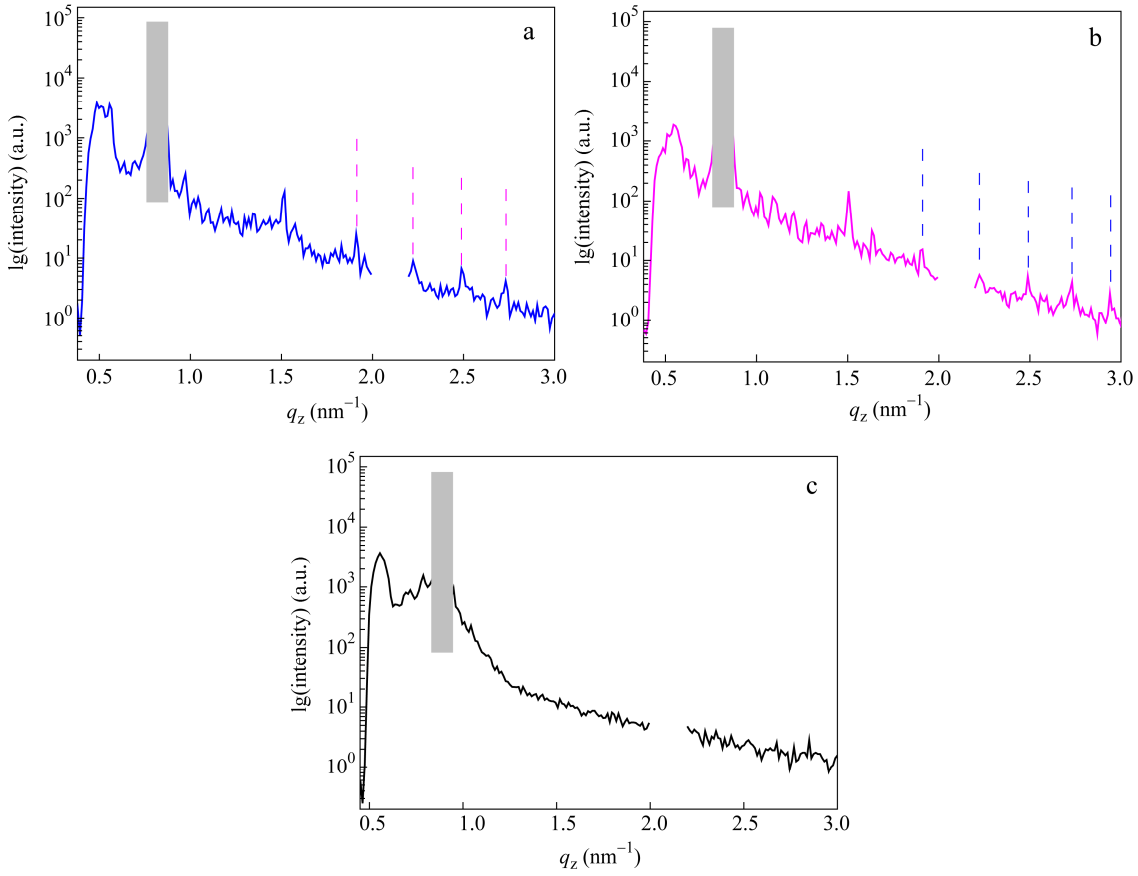


Fig. 7 Vertically integrated nGISAXS data of PS-*b*-PCL thin films at q_y = 0: (a) S-833 with the incident X-ray parallel to the LA, (b) S-833 with the incident X-ray normal to the LA and (c) Thermal-annealed PS-*b*-PCL thin film
The absence of the signal at around q_y = 2.1 nm^{-1} is attributed to the IDG of the detector. The periodic features are indicated with dotted lines.

Finally, we analyze the inherent mechanism for the significantly enhanced crystallization in the micromolded PS-*b*-PCL diblock co-polymer thin films with the decrease of mold size. First of all, the material flow in the imprinted samples is influenced by the geometric confinement of the mold. Large-area dewetting, as observed in the thermal-annealed PS-*b*-PCL thin film, is inhibited. Secondly, the imprinting-induced flow promotes the microstructures of PS-*b*-PCL align along the PDMS wall. Moreover, the selective interaction between PDMS and PS-*b*-PCL leads to the ordering of the polymer. Considering that PDMS has a very low

surface energy, the PCL block which has a lower surface energy than the PS block would aggregate at the PDMS/PS-*b*-PCL interface to minimize the interface energy[18, 37]. The smaller the trench size, the more dominant is this affinity due to the increased contact area and surface-to-volume ratio. Thirdly, the ordering of the PS-*b*-PCL microphase structure in the melt could promote the nucleation of PCL, as the polymer chain at the tethering point could be stretched[21]. The chain interpenetration between PS and PCL is expected to be decreased. This paves the way for the PCL molecules to diffuse towards the crystal growth front[38, 39]. Finally, the PCL crystallization is well confined in the vitreous PS matrix and crystal growth is diffusion-limited (see S1 of Supporting Information). The geometric confinement leads to an enrichment of PCL along the long-axis of the trench. This directs the fast-growth axis of PCL along the same direction. Thus, well aligned crystals were observed in S-566 and S-420 as shown in the azimuthal data in Fig. 4.

Our findings prove that the combination of mesoscale confinement resulting from optical lithography and nanoscale confinement from microphase segregation of block copolymer is a useful tool to control the molecular crystallization. Considering that the crystallization represents the atomic scale length order of material, it establishes the way to fabricate the long-range order nanostructures with high precision in a simple and cost-effective way.

CONCLUSIONS

In this work, the long-range ordered crystalline structure was prepared by micromolding semicrystalline PS-*b*-PCL diblock copolymer thin films. On the basis of a series of complementary characterizing results, we illustrated that micromolding has a great influence on the microphase structure and crystal orientation of PS-*b*-PCL. Significantly enhanced crystallization is reported for the first time. By comparing with the thermally annealed PS-*b*-PCL and imprinted PCL thin films, we inferred that the enhanced crystallization of imprinted PS-*b*-PCL is driven by the surface-induced ordering of PS-*b*-PCL in melt which paves the way for the following crystallization, *i.e.*, enhanced nucleation and fast growth along the LA of the mold. This inference was corroborated with the nanobeam GISAXS experiments, namely, regular lamellae structure and Yoneda peaks for PS and crystalline PCL were observed only in the imprinted PS-*b*-PCL thin films. These findings prove that the long-range ordering of nanostructures at atomic length scale could be achieved by tuning the mesoscale confinement.

ACKNOWLEDGMENTS We thank Perlich Jan (HASYLAB, DESY), Dr. Zhijun Hu (Soochow University) for useful discussions. A portion of this work is based on the data obtained at 1W1A, BSRF, China and P03, DESY, Germany. The authors gratefully acknowledge the assistance of scientists of Diffuse X-ray Scattering and MiNaXS Stations during the experiments.

REFERENCES

1 Grzybowski, B. and Whitesides, G., Science, 2002, *2*95: 2418
2 Park, S., Lee, D.H., Xu, J., Kim, B., Hong, S.W., Jeong, U., Xu, T. and Russell, T.P., Science, 2009, 323: 1030
3 Kim, Y., Cook, S., Tuladhar, S.M., Choulis, S.A., Nelson, J., Durrant, J.R., Bradley, D.D.C., Giles, M., McCulloch, I., Ha, C.S. and Ree, M., Nat. Mater., 2006, 5: 197
4 Liu, F., Gu, Y., Shen, X., Ferdous, S., Wang, H.W. and Russell, T.P., Prog. Polym. Sci. 2013, 38: 1990
5 Briseno, A.L., Mannsfeld, S.C.B., Shamberger, P.J., Ohuchi, F.S., Bao, Z.N., Jenekhe, S.A. and Xia, Y.N., Chem. Mater., 2008, 20: 4712
6 Zhang, P., Huang, H., Yan, D. and He, T., Langmuir, 2012, 28: 6419
7 Kim, Y.Y., Ahn, B., Sa, S., Jeon, M., Roth, S.V., Kim, S.Y. and Ree, M., Macromolecules 2013, 46: 8235
8 Michell, R.M., Blaszczyk-Lezak, I., Mijangos, C. and Muller, A.J., Polymer, 2013, 54: 4059

9 Nakagawa, S., Tanaka, T., Ishizone, T., Nojima, S., Kakiuchi, Y., Yamaguchi, K. and Nakahama, S., Macromolecules, 2013, 46: 2199
10 Hu, Z., Baralia, G., Bayot, V., Gohy, J. and Jonas, A., Nano Lett., 2005, 5: 1738
11 Hu, Z. and Jonas, A.M., Soft Matter, 2010, 6: 21
12 Poelma, J.E. and Hawker, C.J., Nat. Nanotechnol., 2010, 5: 243
13 Park, S.M., Stoykovich, M.P., Ruiz, R., Zhang, Y., Black, C.T. and Nealey, P.E., Adv. Mater., 2007, 19: 607
14 Kim, B.H., Kim, J.Y. and Kim, S.O., Soft Matter, 2013, 9: 2780
15 Kim, S., Nealey, P.F. and Bates, F.S., Nano Lett., 2013, 14: 148
16 Park, S.M., Liang, X.G., Harteneck, B.D., Pick, T.E., Hiroshiba, N., Wu, Y., Helms, B.A. and Olynick, D.L., ACS Nano, 2011, 5: 8523
17 Yi, H., Bao, X.Y., Zhang, J., Bencher, C., Chang, L.W., Chen, X.Y., Tiberio, R., Conway, J., Dai, H.X., Chen, Y.M., Mitra, S. and Wong, H.S.P., Adv. Mater., 2012, 24: 3107
18 Maher, M.J., Bates, C.M., Blachut, G., Sirard, S., Self, J.L., Carlson, M.C., Dean, L.M., Cushen, J.D., Durand, W.J., Hayes, C.O., Ellison, C.J. and Willson, C.G., Chem. Mater., 2014, 26: 1471
19 Zhang, P., Huang, H., He, T. and Hu, Z., ACS Macro Lett., 2012, 1: 1007
20 Zhang, P., Wang, Z., Huang, H. and He, T., Macromolecules, 2012, 45: 9139
21 Nakagawa, S., Kadena, K.i., Ishizone, T., Nojima, S., Shimizu, T., Yamaguchi, K. and Nakahama, S., Macromolecules, 2012, 45: 1892
22 Chatani, Y., Okita, Y., Tadokoro, H. and Yamashit. Y., Polym. J., 1970, 1: 555
23 Crescenzi, V., Manzini, G., Calzolari, G. and Borri, C., Eur. Polym. J., 1972, 8: 449
24 Nojima, S., Ohguma, Y., Kadena, K., Ishizone, T., Iwasaki, Y. and Yamaguchi, K., Macromolecules, 2010, 43: 3916
25 Buffet, A., Rothkirch, A., Dohrmann, R., Korstgens, V., Kashem, M.M.A., Perlich, J., Herzog, G., Schwartzkopf, M., Gehrke, R., Muller-Buschbaum, P. and Roth, S.V., J. Synchrotron Radiat., 2012, 19: 647
26 Muller-Buschbaum, P., Anal. Bioanal. Chem., 2003, 376: 3
27 Quiram, D.J., Register, R.A., Marchand, G.R. and Adamson, D.H., Macromolecules, 1998, 31: 4891
28 Sanandaji, N., Ovaskainen, L., Gunnewiek, M.K., Vancso, G.J., Hedenqvist, M.S., Yu, S., Eriksson, L., Roth, S.V. and Gedde, U.W., Polymer, 2013, 54: 1497
29 Hamilton, B.D., Weissbuch, I., Lahav, M., Hillmyer, M.A. and Ward, M.D., J. Am. Chem. Soc., 2009, 131: 2588
30 Muller-Buschbaum, P., Bauer, E., Pfister, S., Roth, S.V., Burghammer, M., Riekel, C., David, C. and Thiele, U., Europhys. Lett., 2006, 73: 35
31 Muller-Buschbaum, P., Bauer, E., Maurer, E., Roth, S.V., Gehrke, R., Burghammer, M. and Riekel, C., J. Appl. Crystallogr., 2007, 40: S341
32 Al-Hussein, M., Ruderer, M.A., Metwalli, E., Korstgens, V., Vainio, U., Roth, S.V., Dohrmann, R., Gehrke, R., Gebhardt, R., Burghammer, M. and Muller-Buschbaum, P., Macromolecules, 2009, 42: 4230
33 Roth, S.V., Autenrieth, T., Grubel, G., Riekel, C., Burghammer, M., Hengstler, R., Schulz, L. and Muller-Buschbaum, P., Appl. Phys. Lett., 2007, 91: 091915
34 Yarusso, D.J. and Cooper, S.L., Macromolecules, 1983, 16: 1871
35 Sun, Y.S., Chien, S.W. and Liou, J.Y., Macromolecules, 2010, 43: 7250
36 Nojima, S., Fujimoto, M., Kakihira, H. and Sasaki, S., Polym. J., 1998, 30: 968
37 Chaudhury, M.K. and Whitesides, G.M., Langmuir, 1991, 7: 1013
38 Rastogi, S., Lippits, D.R., Peters, G.W.M., Graf, R., Yao, Y. and Spiess, H.W., Nat. Mater., 2005, 4: 635
39 Shin, K., Obukhov, S., Chen, J., Huh, J., Hwang, Y., Mok, S., Dobriyal, P., Thiyagarajan, P. and Russell, T., Nat. Mater., 2007, 6: 961